Real-time, chirped-pulse heterodyne detection at room-temperature with 100GHz 3dB-bandwidth mid-infrared quantum-well photodetectors

Quyang Lin, Michael Hakl, Sylvie Lepilliet, Hua Li, Jean-Francois Lampin, Emilien Peytavit, Stefano Barbieri

Real-time, chirped-pulse heterodyne detection at room-temperature with 100GHz 3dB-bandwidth mid-infrared quantum-well photodetectors

QUYANG LIN,[1] MICHAEL HAKL,[1] SYLVIE LEPILLET,[1] HUA LI,[2] JEAN-FRANÇOIS LAMPIN,[1] EMILIEN PEYTAVIT[1] AND STEFANO BARBIERI[1,*]

[1] *Institute of Electronics, Microelectronics and Nanotechnology, CNRS, Univ. Lille, Univ. Polytechnique Hauts-de-France, UMR 8520, F-59000 Lille, France*
[2] *Key Laboratory of Terahertz Solid State Technology, Shanghai Institute of Microsystem and Information Technology, Chinese Academy of Sciences, 865 Changning Road, Shanghai 200050, China*
[*] *stefano.barbieri@iemn.fr*

Abstract: Thanks to intrinsically short electronic relaxation on the ps time scale, III-V semiconductor unipolar devices are ideal candidates for ultrahigh-speed operation at mid-infrared frequencies. In this work, antenna-coupled, GaAs-based multi quantum-well photodetectors operating in the 10-11μm range are demonstrated, with a responsivity of 0.3A/W and a 3dB-cutoff bandwidth of 100GHz at room-temperature. The frequency response is measured up to 220GHz: beyond 100GHz we find a roll-off dominated by the 2.5 ps-long recombination time of the photo-excited electrons. The potential of the detectors is illustrated by setting up an experiment where the time dependent emission frequency of a quantum cascade laser operated in pulsed mode is measured electronically and in real-time, over a frequency range >60GHz. By exploiting broadband electronics, and thanks to its high signal-to-noise ratio, this technique allows the acquisition, in a single-shot, of frequency-calibrated, mid-infrared molecular spectra spanning up to 100GHz and beyond, which is particularly attractive for fast, active remote sensing applications in fields such as environmental or combustion monitoring.

1. Introduction

The quest for broadband photodetectors in the mid-infrared (MIR - λ=3-12 μm), with radio-frequency (RF) bandwidths in the tens of GHz or more, has gained momentum since the end of the 80s with the advent of unipolar devices based on intersubband (ISB) transitions in III-V semiconductor heterostructures (GaAs/AlGaAs and InGaAs/InAlAs) [1]. Thanks to ultrafast electronic non-radiative lifetimes, these structures offer intrinsic response times in the ps range, potentially leading to RF-bandwiths of tens of GHz, provided that the detector RC time constant is short enough [2–7]. In this respect, the recent exploitation of metallic antennas of micrometric size to in-couple the impinging mid-IR radiation to the semiconductor heterostructure active region, has opened new perspectives by allowing to shrink the detectors area, without compromising the light collection efficiency [8, 9]. On the one hand, compared to standard detectors based on so-called “mesa" geometry, this allows reducing the detector’s dark current without affecting the responsivity. The other advantage is a reduction of the RC time constant, which can be exploited to increase the device speed [6].

In the first part of this work we have pushed forward the study and optimisation of antenna-coupled MIR quantum-well infrared photodetectors (QWIPs), in order to improve their performance both in terms of responsivity and bandwidth, and, at the same time, to try assessing experimentally what are their limiting factors. To this end we have fabricated and characterised experimentally three sets of GaAs/AlGaAs-based QWIPs, based on two-dimensional matrices of metallic patch-antennas, and measured their frequency response at room-temperature in the 0-110GHz and 140GHz-220GHz frequency bands. Depending on the number of antenna

elements, we find that the latter remains within 3dB up to 100GHz (3×3 and 2×2 matrices), the broadest bandwidth reported to date for photodetectors based on ISB transitions. At higher frequencies we find a roll-off between 7 and 9dB/octave. By fitting the frequency response with the help of a small-signal circuit model that we extract from impedance measurements, we conclude unequivocally that the high frequency roll-off is limited by the intrinsic carrier's capture time, of ~ 2.5ps.

By optimizing the QWIPs design, a maximum responsivity of 0.3 A/W is obtained at 10.3μm wavelength, a value significantly larger than what previously reported for patch-antenna QWIPs at 300K (~ 0.15-0.2A/W) [6, 8]. The responsivity decreases with increasing incident optical power, a fact that we attribute to optical saturation of the ISB transition [10, 11]. The corresponding saturation intensity, of only a few tens of kW/cm^2, is consistent with the fact that the antennas allow to obtain a radiation collection area that is larger than the physical area of the detector [12].

Applications of ultrafast QWIPs are only at their early stage, with many exciting developments in disparate fields, such as free-space communications [13–18], gas sensing and spectroscopy [19–26], metrology [27, 28], ultrafast physics [29], and astrophysics [30–32]. In the second part of this work, to assess the potential of our QWIPs for fast sensing/spectroscopy applications, we have used them to detect the heterodyne beating between a quantum cascade laser (QCL) operated in pulsed mode and another one driven in continuous wave (CW). In this way, with the help of a fast oscilloscope, we show that it is possible to measure in real-time the frequency down-chirp resulting from the thermal transient of the pulsed QCL, spanning a range of more than 60GHz. By allowing the acquisition of frequency-calibrated gas spectra with a high signal-to-noise ratio in a single-shot, over timescales from tens of ns to ms, this technique appears to be particularly promising for active remote sensing and laser ranging applications.

2. Results

2.1. Spectral characterisation and device responsivity

The QWIP semiconductor active region consists of six, 6nm-thick, n-doped GaAs quantum wells (QWs) separated by 40nm-thick, undoped $Al_{0.2}Ga_{0.8}As$ barriers, yielding a nominal bound to quasi-bound ISB transition energy of ~ 115meV (λ ~ 10.8μm). Details on the heterostructure layers and device fabrication are given in Methods. The final device geometry is a matrix of square metallic (Ti/Au) patches of side s and separated by a period p. Around each patch the semiconductor is etched down to a bottom metallic ground-plane. As shown in the SEM pictures in Fig. 1(a) the patches are electrically connected together, and to a 50Ω microwave coplanar line for RF extraction, by ~ 150nm wide, Ti/Au wire air-bridges.

In this work we have studied matrices with different number of patches in order to probe the effect on the photodetectors RC time constant. The devices are based on a 5×5 and a 3×3 matrix of period p = 5μm, and a 2×2 matrix of period p = 10μm, that we label M5, M3 and M2 respectively. For all the devices s = 1.8μm. This parameter defines the frequency of the fundamental TM_{010} mode of a single resonator, the one we are interested in, which is, essentially, a $\lambda/2$ Fabry-Perot mode oscillating in the plane of the patches, perpendicularly to the connecting wire bridges [33, 34]. The TM_{100} mode oscillating in the orthogonal direction is instead perturbed by the wire bridges (despite their small size), leading to a lower overlap with the QWIP active region, and therefore a weaker absorption [6].

For a given s, changing the periodicity p affects the radiation collection area of each individual patch in the array [35, 36]. The experimental characterisation and optimisation of the optical absorption of the patch-antenna arrays, made with the help of a MIR microscope coupled to a Fourier transform (FTIR) spectrometer, was carried out over a large number of matrices by varying s and p. The main results are summarised in Supplement 1. In the case where the optical excitation area is smaller than the surface of the matrix (i.e. "infinite" matrix approximation), for the TM_{010} mode we find peak absorptions at ~ 10.5μm (i.e. virtually coincident with the nominal

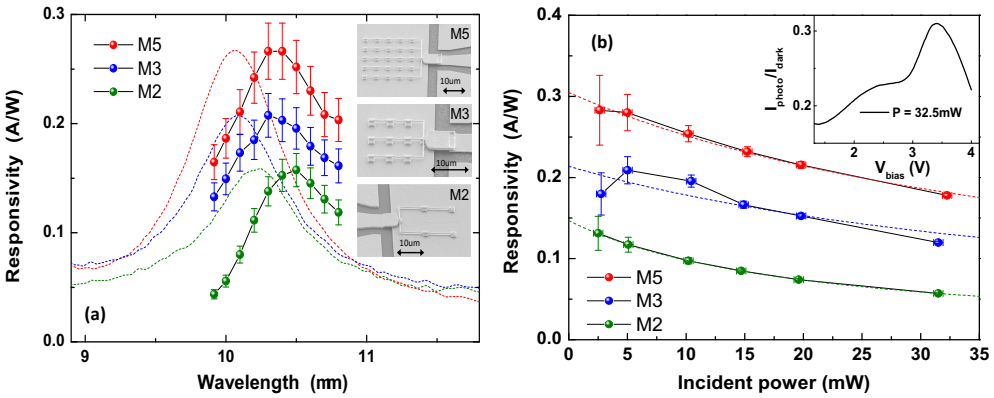

Fig. 1. (a) Room-temperature responsivity *vs* wavelength of the QWIPs studied in this work, measured with an extended-cavity QCL (dots). The incident power is of 4.3mW. For comparison, the absorption spectrum of each device measured with an FTIR spectrometer, normalised to its peak responsivity is also reported (dashed lines). The devices are labelled respectively M5, M3 and M2, and their SEM pictures are shown on the right. For all of them the patches consist of metallic squares of lateral side $s = 1.8\mu$m. In the M5 and M3 devices, individual patches are separated by a period $p = 5\mu$m, while for device M2 we used $p = 10\mu$m. As shown in the pictures, patches are electrically connected together and to a 50Ω integrated coplanar line by a suspended gold wires of ∼ 150nm diameter (only the first part of the coplanar line is visible in the SEM images). (b) Responsivity *vs* incident power at $\lambda = 10.3\mu$m for the 3 devices studied, measured at 300K. The applied biases are 3.9V (devices M5 and M3) and 3.75V (device M2). The error bars take into account the uncertainty in the measurement of the incident power ($\sim \pm 0.4mW$). The dashed lines are the fits of the responsivities using the function $R = R_0/(1 + P_{inc}/P_{sat})$ (see the main text). Inset. Device M5: ratio between the photocurrent at 32.3mW incident power and the dark current.

wavelength of the ISB transition) of 96% and 40% for $p = 5\mu$m and $p = 10\mu$m respectively. In the former case we are therefore very close to so-called “critical" coupling (100% peak optical absorption). The reason why we choose $p = 10\mu$m for device M2, is the results of a compromise between the need to keep a sizeable antenna collection area while having a reasonable spatial overlap with the waist of the focused QCLs used throughout this work, of approximately 25μm diameter (see below).

The room-temperature responsivity of the devices *vs* wavelength in the range 9.9μm-10.8μm, obtained with an extended cavity (EC) QCL polarized perpendicularly to the connecting wires is reported in Fig. 1(a) (dots), for an incident power of 4.3mW. The QCL beam was focused with an AR coated aspheric chalcogenide-glass lens (NA = 0.56; 5 mm focal length), yielding a waist diameter of $\sim 25\mu$m, that we measured with a razor blade. We obtain a maximum responsivity close to 0.3A/W at 10.3μm for device M5. As expected the responsivity is reduced by decreasing the number of patches. Indeed the waist area roughly matches that of a 5×5 matrix. As a consequence, especially for devices M3 and M2, part of the incident radiation is directly reflected by the metallic ground-plane.

The dashed lines in Fig. 1(a) represent the experimental optical absorption for each device, normalised to its peak responsivity (Supplement 1). The observed systematic red shift between the peak absorption and peak responsivity is a consequence of the fact that the QWIP ISB transition energy is not perfectly coincident with the energy of the TM_{010} cavity mode. The

QWIP absorption can be computed analytically using Coupled Mode Theory (CMT) [12, 35, 37]: for device M5 we find a good agreement with the experimental absorption spectrum assuming an ISB transition energy E_{isb} = 115 meV and a cavity mode energy of E_{cav} = 122.5meV (Supplement 1). This gives an external quantum efficiency of ~ 15% for detector M5. We note that in the case where the ISB transition energy was perfectly coincident with that of the cavity mode ($E_{isb} = E_{cav}$ = 122.4meV), this value would raise to ~ 25%, with a corresponding peak responsivity of ~ 0.5A/W.

As reported in Fig. 1(b), the responsivity of the devices measured at $\lambda = 10.3\mu$m displays a sizeable decrease (up to ~ 40 − 60% depending on the number of patches) with increasing power. In Ref. [12] it was shown that the optical saturation intensity of an ISB transition system can be strongly reduced if the latter is embedded inside an optical cavity of sub-wavelength volume, as is the case here. Using CMT, we compute a saturation intensity for our patch-antenna I_{sat} ~ 35kW/cm^2 at $\lambda = 10.3\mu$m. To estimate the corresponding incident saturation power, P_{sat}, we must take into account the fact that each patch-antenna in the array collects photons on a surface larger than its physical area. As a result, at critical coupling, the incident saturation intensity is obtained by multiplying I_{sat} by the factor s^2/p^2 (Supplement 1). Considering a waist diameter of ~ 25μm, and taking into account the different peak absorptions of each detector we finally obtain P_{sat} ~ 30mW, 45mW, and 20mW for QWIPs M5, M3 and M2 respectively. The dashed lines in Fig. 1(b) represent the fits of the responsivities using the function $R = R_0/(1 + P_{inc}/P_{sat})$, where P_{inc} is the incident power and R_0 and P_{sat} are used as fitting parameters (R_0 is the responsivity at low incident power) [12]. From the fits we obtain P_{sat} = 47 ± 3mW, 50 ± 20mW and 20 ± 0.1mW for QWIPs M5, M3 and M2 respectively, in fairly good agreement with the computed values.

2.2. *Frequency response*

The experimental setup for the measurement of the QWIPs frequency response is based on the heterodyne mixing of a DFB QCL emitting at ~ 10.3μm with an EC QCL (the same used for Fig. 1(a)). Both lasers are operated in CW, and a MIR isolator is used to minimise optical feedback. As a consequence the incident radiation is linearly polarised along the diagonal of the square patches, resulting into a ~ 50% drop of absorption compared to Fig. 1. The incident powers on the QWIPs are P_1 = 13mW and P_2 = 17.5mW from the EC and DFB QCLs respectively. To avoid parasitic effects due to wire-bonding/packaging, the measurement of the heterodyne signal, oscillating at the difference between the emission frequencies of the two QCLs, is done directly on-wafer by positioning two sets of coplanar probes at the the edge of the integrated 50Ω coplanar line, followed by a bias-tee and a calibrated power meter covering respectively the 0-110GHz and 140GHz-220GHz frequency bands.

In Fig. 2 we report representative experimental frequency response functions for devices M5, M3 and M2, obtained by sweeping the emission frequency of the EC QCL using the external grating, while the DFB QCL is kept at constant current. The devices are biased at 3.8V (M5), 3.85V (M3) and 4V (M2), corresponding to the maximum generated photocurrents (Supplement 1). The experimental power values are corrected by the attenuation of the bias-tees and coplanar probes, measured with a Vector Network Analyser (VNA). We obtain 3dB cutoffs of ~ 90GHz for device M5 and of ~ 100GHz for devices M3 and M2 (the cutoffs are defined relatively to the peak response). These are the largest bandwidths reported to date in the literature for unipolar MIR photodetectors and, more generally, for MIR photodetectors. Beyond the 3dB cutoff the response drops by approximately 8dB/octave.

The frequency response of the photodetector is essentially the product of two transfer functions, the first including the electrical response, while the second one takes into account the intrinsic response time of the photo-excited electrons [1]. To obtain the electrical response functions of the devices studied, we first measured their impedance and then used the latter to derive an

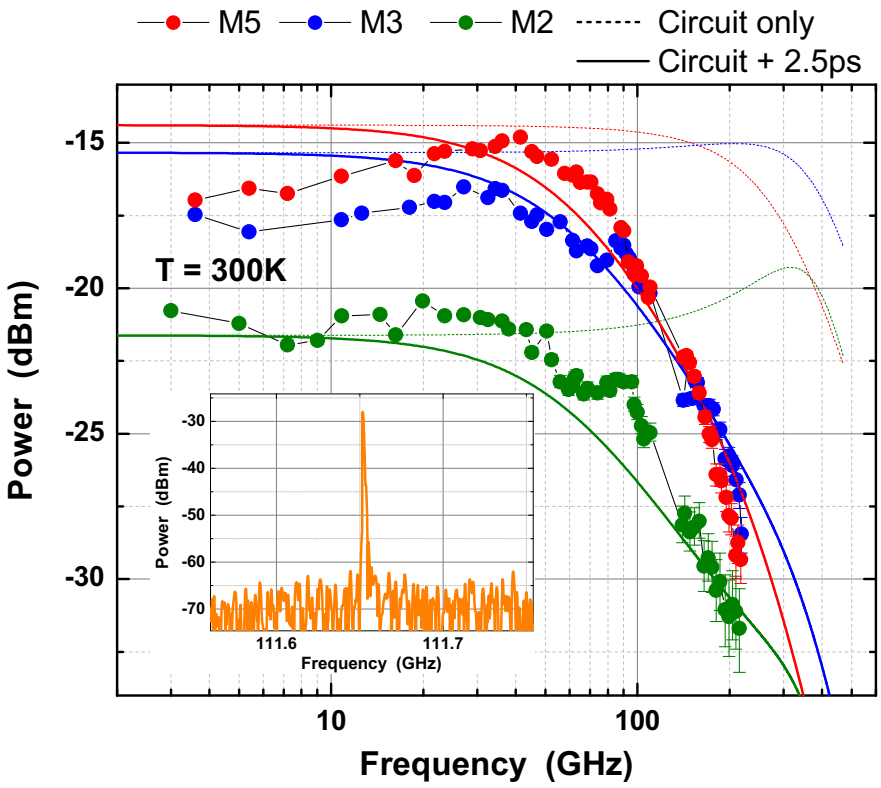

Fig. 2. (a) Room-temperature experimental frequency response of devices M5 (red dots), M3 (blue dots) and M2 (green dots) in the frequency bands 0-110GHz and 140-220GHz. The measurement are obtained at $\lambda \simeq 10.3\mu$m by heterodyne mixing two single-mode QCLs, and the experimental values are corrected by the attenuation of the bias-tees and coplanar probes, measured with a VNA. All data was recorded without the use of any amplification stage. The incident MIR radiation is linearly polarised at 45deg with respect to the metallic wires connecting the patches, and the incident powers are 13mW and 17.5mW. The corresponding *dc* photocurent are 4.1mA, 2.8mA, and 1.25mA for devices M5, M3 and M2 respectively. The dashed lines are the computed electrical frequency responses obtained from the small-signal equivalent circuit (Supplement 1, Fig. S4). The solid lines include the intrinsic ISB frequency response with a carrier capture time of 2.5ps. Inset. Example of heterodyne beatnote close to 110GHz, recorded with a spectrum analyser using the M3 photodetector. The spectrum is not corrected by the attenuation through the 110GHz probe and bias-tee.

equivalent small-signal circuit model (Supplement 1). The frequency response can then be obtained by computing the average power, $P_L(\omega)$ dissipated in the 50Ω input impedance of the power meter, where ω is the difference frequency between the two QCLs, and considering an ac current source term of amplitude I_s proportional to the total dc photocurrent generated by the two QCLs (Methods). The dashed lines in Fig. 2 are the so-obtained electrical frequency responses. Clearly, the predicted cutoff frequencies are much larger than those observed experimentally, i.e. the response time of our photodetectors is not limited by the electrical time constant but rather by the intrinsic response time of the ISB system, which can be taken into account by multiplying the electrical transfer function by the term $[1 + (\omega\tau)^2]^{-1/2}$, where τ represents the shortest between the carriers capture time and transit time [1]. The best agreement with the experimental frequency responses is shown by the solid lines in Fig. 2, obtained with $\tau = 2.5$ps, that we identify with the carriers capture time. Indeed, under the experimentally applied biases we estimate a drift velocity at room temperature of $2 - 3 \times 10^6$ cm/s, yielding a transit time of $\sim$ 10ps [6, 9].

2.3. Heterodyne frequency-chirp spectroscopy

It is well-known that driving a QCL in pulsed mode generates a down-chirp of the emission frequency of thermal origin, that can reach up to several tens of GHz. This effect can be exploited to detect in real time different gas species for applications in environmental and combustion monitoring, plasma diagnostic, or high-resolution spectroscopy [38–44].

In a typical experiment, the beam emitted by a pulsed QCL is transmitted through a gas cell, then focused on a detector of sufficiently high speed to resolve the optical pulse, which is finally connected to an oscilloscope. The resulting electrical pulse will display a number of dips generated each time the QCL frequency goes across a molecular absorption line. One weak point of this technique is that the value of the QCL emission frequency at each instant of time during the pulse is not known, a fact that can be problematic, for instance for the determination of unknown transition lines. For sufficiently short driving pulses the frequency chirp is approximately linear, allowing an absolute frequency pre-calibration using a Fourier transform (FT) spectrometer [40]. The generation of wider frequency spans requires instead longer driving pulses, typically ranging from tens of μs to several ms, during which the time dependence of the QCL frequency is highly non-linear, requiring the use of an etalon for real-time relative frequency calibration [41]. An alternative solution to this problem is offered by the 100GHz bandwidth of our QWIP, giving the possibility to measure in real-time the relative emission frequency of a pulsed QCL through heterodyne detection.

The schematic of the heterodyne frequency-chirp spectroscopy (HFCS) experimental setup exploiting the same QCLs used to characterise the QWIPs frequency response is shown in Fig. 3. The $\sim$ 10.3μm-wavelength DFB QCL is driven in pulsed mode, with 3.5ms-long pulses and 100Hz repetition rate, producing a frequency down-chirp of approximately 60GHz (see below). The emitted optical beam is transmitted through a 8cm-long gas cell containing NH_3 and finally focused on a QWIP nominally identical to the M5 device of Fig. 1(a). The tunable EC QCL is driven in CW and directly focused on the QWIP to provide the local oscillator for heterodyne detection. Its absolute frequency is monitored with a Fourier transform-based λ-meter with a frequency resolution of 1GHz. As for the characterisation of the frequency response, an optical isolator (not shown in the figure) is placed before the QWIP. The QWIP is in series with a 34Ω resistor, and is connected to a 67GHz bias-tee. The dc port of the latter is used to bias the QWIP with a dc power supply ($\sim$ 4.5V applied bias - not shown in the Figure). Simultaneously, we measure the voltage across the 34Ω resistor, proportional to the QWIP current, with the help of a 200MHz bandwidth oscilloscope. The ac port of the bias-tee is connected to a 70GHz bandwidth oscilloscope, allowing to measure in real-time the heterodyne frequency pulse resulting from the mixing between the DFB and the EC QCLs. As for the heterodyne measurement of the frequency response, we note the absence of any RF amplification stage in this experimental setup.

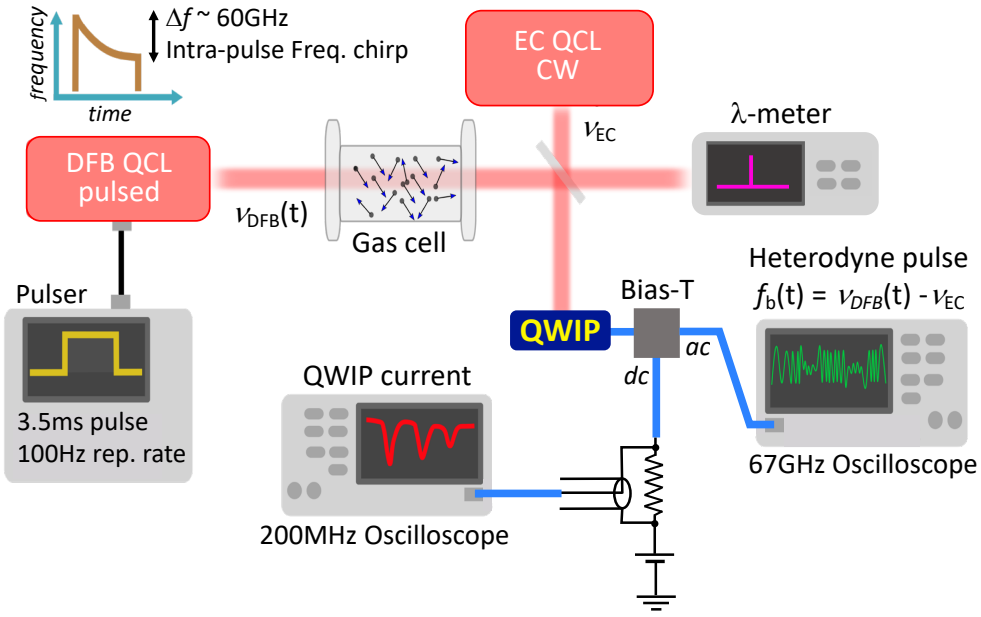

Fig. 3. Schematic of the HFCS experiment (see main text for more details). A DFB QCL, with emission frequency ν_{DFB}(t), is driven in pulsed mode, producing a frequency down-chirp of approximately 60GHz. Its beam is transmitted through a gas cell containing NH_3 and focused on the QWIP. A tunable EC QCL is driven in CW and provides the local oscillator for heterodyne detection. Its absolute frequency, ν_{EC}, is monitored with a λ-meter. The QWIP, in series with a 34Ω resistor, is connected to a 67GHz bias-tee and biased with a *dc* power supply. A 200MHz bandwidth oscilloscope is used to measure the voltage across the 34Ω resistor, proportional to the QWIP current. The *ac* port of the bias-tee is connected to a 70GHz bandwidth oscilloscope, which measures in real-time the heterodyne frequency pulse, oscillating at $f_b(t) = \nu_{DFB}(t) - \nu_{EC}$, resulting from the mixing between the DFB and the EC QCLs.

An example of heterodyne pulse, recorded in single-shot with the gas cell empty, is shown in the inset of Fig. 4(b) (see the Figure caption for the QCLs driving conditions and the power incident on the QWIP). The heterodyne amplitude oscillations cannot be resolved directly using the full chirped pulse since the latter does not contain a sufficiently large number of points. The instantaneous frequency is therefore obtained by measuring, at different instants of time, single-shot, 10ns-long time traces, and by computing their Fourier transform in real time with the help of the 70GHz oscilloscope. This gives rise to the type of RF spectra shown in Fig. 4(a) obtained, without gas cell, from a chirped pulse different from the one shown in the inset (see caption of Fig. 4). As shown by the one highlighted in blue in the Figure, each RF spectrum consists of a main peak followed by a few low power harmonics, with the former corresponding to the instantaneous beat frequency between the DFB and EC QCLs emission frequencies: $f_b(t) = \nu_{DFB}(t) - \nu_{EC}$. As shown by the top arrow, from 0ms to 3.5ms $f_b(t)$ spans approximately 60GHz. We note the high dynamic range obtained (up to 60dB) despite the fact that the chirped pulse is acquired without amplification and in single-shot. Indeed, we found that the introduction of an averaging produced a reduction of the pulse amplitude that we attribute to the frequency fluctuations of the EC QCL operating in free-running, automatically transferred to

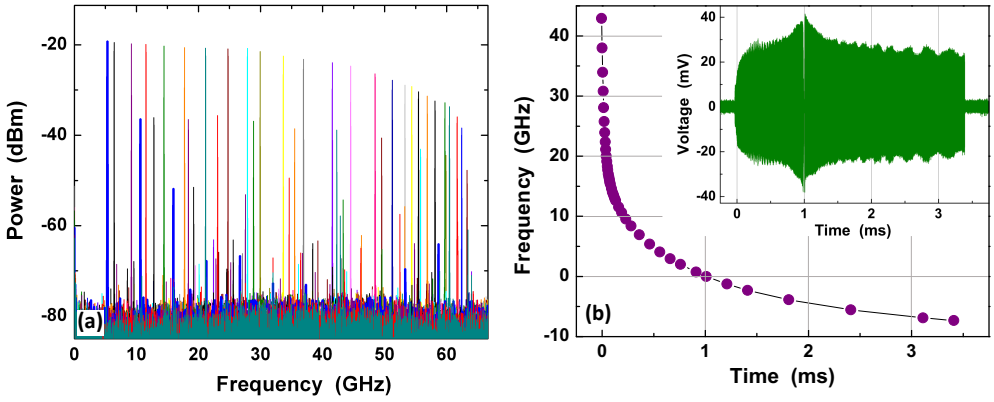

Fig. 4. (a) Example of heterodyne spectra obtained by computing, in real time, the FFT of a chirped pulse over a 10ns-long sliding temporal window. Time increases from right to left as schematically shown by the top arrow. For clarity, the lowest frequency spectrum is displayed in blue, showing the fundamental oscillation, close to 5GHz, and a few lower power harmonics, stemming from the QWIP I/V non-linearity and/or a circuit non-linearity (Supplement 1) [45] The chirped pulse is different from the one shown in the inset of panel (b), with the QCLs operating conditions set to obtain always a positive $f_b(t)$. The pulse was recorded without gas cell, yielding $\sim$ 15mW of peak and CW power incident on the QWIP. (b) Beat-frequency *vs* time obtained from the heterodyne chirped pulse shown in the inset. The frequency was obtained by recording the same type of heterodyne spectra shown in panel (a). Inset. Single-shot chirped pulse obtained by driving the DFB QCL at 23.8°C with 3.5ms-long 995mA pulses, and 100Hz repetition rate. The beam of the DFB QCL is transmitted through the empty gas cell, producing a $\sim$ 30% power attenuation. The EC QCL is driven in CW at 1A and 17.8°C yielding an emission frequency 29004.6 GHz (10.343μm). The peak and CW power incidents on the QWIP are of approximately 10mW.

$f_b(t)$. This problem could be solved by locking the EC QCL to a more stable reference [27, 28].

The temporal evolution of $f_b(t)$ is highly non-linear. This is shown in Fig. 4(b), reporting the beat frequency as obtained from the chirped-pulse in the inset. The observed down-chirp is of pure thermal origin and reflects the heating of the active region due to the applied current pulse. As discussed in Ref. [42] this process involves several time constants, corresponding to joule heating diffusing through the laser active region, waveguide, substrate etc. We note that close to 1ms, $f_b(t)$ goes through zero, which corresponds to the point where the DFB and EC QCLs frequencies are equal. This produces a smooth peak in the envelope of the heterodyne pulse, since as f_b moves away from dc, we have an increase of the microwave propagation losses of the 1m-long, 67GHz coaxial cable connecting the ac port of the bias-tee to the 70GHz oscilloscope. Adding the emission frequency of the EC QCL measured with the λ-meter to the heterodyne frequency of Fig. 4(b) provides the temporal evolution of the DFB QCL absolute emission frequency. This can then be used as a calibration for HFCS.

The result of a proof-of-principle HFCS experiment is shown in Fig. 5, obtained by filling the gas cell with pure NH_3 at a nominal pressure of 100Pa. The top panel shows the chirped-frequency pulse, while the current pulse measured on the dc port of the bias-tee is reported in the bottom panel, together with the pulse without gas for comparison. In both time-traces, several absorption dips are visible, corresponding to NH_3 absorption lines, while the spike at $\sim$ 1ms in the QWIP current is an experimental artefact produced by $f_b(t)$ passing through 0. It is worth noting that, contrary to the chirped pulse, recorded in single-shot, the current pulse is obtained by averaging

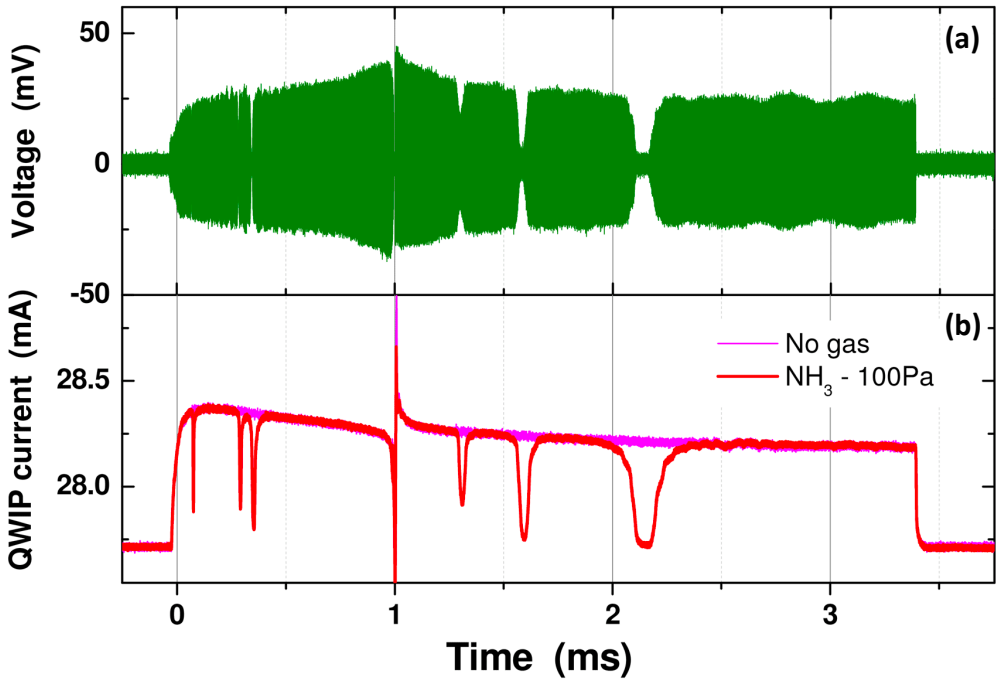

Fig. 5. (a) Single-shot chirped-frequency pulse obtained by driving the QCLs under the same conditions used for Fig. 4(b). The beam from the pulsed DFB QCL is transmitted through the gas cell filled with NH_3 at a nominal pressure of 100Pa. (b) Current pulse measured on the *dc* port of the bias-tee (see Fig. 3), with the gas cell empty (purple) and filled with NH_3 (red).

over 100 time-traces (see Methods for a comparison between the chirped pulse and the current pulse in single-shot, and for the pressure detection limit).

The solid green line in Fig. 6 represents the NH_3 transmission spectrum extracted from the heterodyne pulses, where the time axis has been replaced by the absolute frequency of the chirped QCL based on the linear interpolation of the frequency *vs* time curve displayed in Fig. 4(b). The spectrum is the result of the ratio between the squares of the voltage heterodyne pulses (proportional to the transmitted power) with and without gas (the pulse with gas is the one displayed in Fig. 5(a)). To remove the heterodyne oscillations both time traces where numerically averaged. For comparison, the red line shows the NH_3 spectrum derived from the ratio between the current pulses with and without gas of Fig. 5(b). As expected, the frequencies of the absorption lines in the two spectra are perfectly coincident. The orange stars represent the frequencies and the transmission intensities of the closest NH_3 ro-vibrational transitions, based on the HITRAN database and computed with the commercial software Spectracalc®, using a gas pressure of 90Pa and a 8-cm gas cell length, i.e. equal to the nominal one. The agreement with the computed line intensities is very good, considering that the difference with the nominal gas pressure of 100Pa is within the measurement error. In Table I we report the HITRAN and measured frequencies, showing that for all the lines except the highest frequency one, we find a nearly constant shift of ~ 600MHz that is within the resolution (1GHz) of the λ-meter used to measure the frequency of the CW QCL. The reason why the saQ(1,1) transition is shifted by only 300MHz could be due to a drift of the EC QCL during the acquisition of the chirped frequency values displayed in Fig. 4(b), which were necessarily measured at different times. Further measurements would be needed to clarify this point, which is however outside the scope

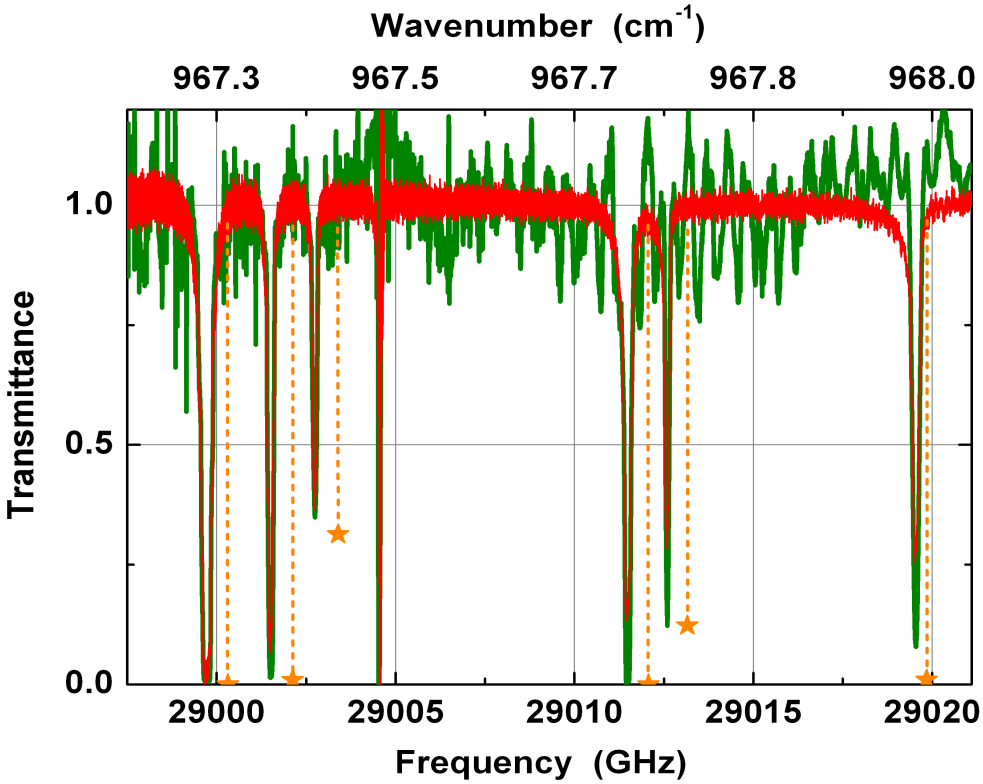

Fig. 6. Green line. NH_3 transmission spectrum obtained from the ratio between the squares of the heterodyne pulses with and without gas (the pulse with gas is the one displayed in Fig. 5(a)). Red line. NH_3 spectrum derived from the ratio between the current pulses with and without gas of Fig. 5(b). The orange stars represent the frequency and the transmission intensities of the closest NH_3 ro-vibrational transitions, based on the HITRAN database and computed with the commercial software Spectracalc®.

of this work. On this issue, it is anyway important to note that the frequency calibration procedure based on the linear interpolation of the data-points of Fig. 4(b), which has been used here for illustrative reasons, is not strictly necessary. Indeed, a faster and possibly more precise way of determining the absolute frequency of a given transition line, is to directly measure the value of the chirped frequency by using a 10-ns time-window positioned right on top of corresponding transmission dip (after removing the gas if the transmission is too low).

The higher noise visible in the green spectrum compared to the red one, is partly due to slow amplitude oscillations in the heterodyne pulse, due to standing-wave effects (see Fig.4(b)) that could not be completely removed by the normalisation process. Another source of noise is due to the QCLs loosing their coherence, giving rise to short random frequency fluctuations. This problem should be removed by stabilising the two lasers sources. Finally, in Fig. 6, we observe that corresponding to the three highest frequency NH_3 transition lines, the red spectrum shows a systematically higher transmission compared to the green one, as well as a slight line asymmetry. We attribute this facts to the finite transient response time of the voltage source used to bias the QWIP, effectively limiting the current rise time when the frequency of the pulsed QCL sweeps across the absorption lines (see Methods). This experimental artifact is not present on the *ac* port of the bias-tee, where slow bias variations are filtered out, yielding a transmission spectrum with perfectly symmetrical lines (see Supplement 1 for a comparison between the transmittance

of all the measured transitions as obtained from the chirped pulse, with those computed with Spectracalc®).

3. Conclusions

In this work we have demonstrated that antenna-coupled MIR unipolar quantum-well photodetectors based on ISB transitions can reach a 3dB RF bandwidth of 100GHz at room temperature, with a responsivity of $\sim$ 0.3A/W at 10.3μm wavelength. By fabricating and characterising photodetectors containing different numbers of patch-antennas we have demonstrated that the high frequency cutoff is not limited by the device parasitics, but rather by the intrinsic properties of the semiconductor heterostructure itself, namely the carriers capture time, of the order of 2.5ps.

Thanks to their ultra-broad bandwidth we believe that the demonstrated detectors are particularly appealing as heterodyne receivers for applications as diverse as MIR astronomy, light detection and ranging (LIDAR), spectroscopy or free-space communications [4,13–15,17,19–22,25,30–32]. Indeed operating these devices as direct detectors at room temperature is less attractive due to their high dark current. Instead, besides the obvious benefits of coherent detection, adopting a heterodyne configuration gives in principle the possibility to reach a detection limited by the photon noise if the local-oscillator photocurrent is larger than the thermally activated dark current. As shown in the inset of Fig. 1(b), at the actual operating wavelength of $\sim$ 10μm, this seems out of reach at T=300K, due to the elevated dark current and to the observed decrease of the responsivity with increasing power that we interpret as the result of a partial optical saturation. This phenomenon was never observed before in a QWIP [10,11,46] and is, in a way, the drawback of coupling the ISB structure to an antenna, which permits to achieve a higher detectivity at the price of a lower saturation power [11, 12]. Although I_{sat} can be increased by increasing the doping in the QWs (Supplement 1), however, according to our estimates, this gain would be quickly compensated by the growth of the dark current which depends exponentially on n_s. On the other hand, preliminary data as a function of temperature indicate that it should be possible, with the present detector, to achieve a shot-noise limited detection in proximity of T=250K (or possibly higher in the case where the frequencies of the ISB transition and of the patch resonators were perfectly matched, see Section 2.1), which can be reached with a thermoelectric cooler. In terms of RF bandwidth, although the present 100GHz is probably enough for most applications, a possibility to improve it would be to reduce the capture time, for instance by reducing the barriers

Table 1. NH_3 ro-vibrational transitions. The table reports the line center frequencies, rounded to 0.1 GHz, obtained from the HITRAN database and from Fig.6(b). Δf is their difference.

Transition	Frequency (GHz)		
	HITRAN	This work	Δf
saQ(3,3)	29000.3	28999.7	0.6
saQ(3,2)	29002.1	29001.5	0.6
saQ(3,1)	29003.4	29002.7	0.7
saQ(2,2)	29012.1	29011.5	0.6
saQ(2,1)	29013.2	29012.6	0.6
saQ(1,1)	29019.8	29019.5	0.3

width which, at the moment is comparable to the estimated carrier's mean free path [1]. In this respect we note that an experimental study on the dependence of MIR patch-antenna QWIPs performance (e.g. responsivity, bandwidth etc) on parameters such as the active region thickness or the number of QWs is presently lacking [36].

To demonstrate the potential of our detectors as heterodyne receivers we have setup a proof-of-principle experiment where the chirped-frequency emitted by a QCL driven in pulsed mode is down-converted in the microwave range through the mixing with a second QCL operated in CW. In this way it is possible to record in real-time molecular spectra spanning up to 100GHz (and beyond), limited by the bandwidth of our detector. Contrary to conventional chirped pulsed spectroscopy, our HFCS technique simplifies the absolute calibration of the chirped frequency. Most importantly it permits to achieve high SNRs ($\sim$ 60dB in 100MHz bandwidth with $\sim$ 15mW of peak and CW power respectively from the pulsed and CW QCLs - see Fig. 4(a)), which in our opinion, makes patch-antenna QWIPs particularly attractive for remote sensing applications and also free-space communications. In particular the reported high SNR shows that the pulsed QCL beam should still be detectable after propagating through the atmosphere by several tens of km in adverse weather conditions [47].

To this end we note that much higher SNRs could be reached by locking the CW QCL to a more stable reference such as a frequency comb, or by replacing it with an intrinsically more stable MIR source such as a CO_2 laser.

4. Methods

4.1. Devices structure and fabrication

A 100nm-thick, lattice-matched $Ga_{0.51}In_{0.49}P$ etch-stop layer followed by the $Al_{0.2}Ga_{0.8}As$/GaAs heterostructure is grown by MBE on top of a semi-insulating GaAs substrate. The heterostructure is sandwiched between 50 and 100nm-thick top and bottom n-doped contact layers with concentrations $3 \times 10^{18}cm^{-3}$ and $4 \times 10^{11}cm^{-3}$, and consists of six, 6nm-thick GaAs QWs with the central 5nm *n*-doped at $6 \times 10^{17}cm^{-3}$, separated by 40nm-thick, undoped $Al_{0.2}Ga_{0.8}As$ barriers.

The epi-layer is first transferred onto a 2"-diameter high-resistivity Si wafer using Au–Au thermo-compression bonding. The fabrication begins by wet etching the GaAs substrate and the etch-stop layer. Next, a Ti/Au (8nm/300nm) top Schottky contact is realized through e-beam lithography, followed by e-beam evaporation and lift-off. The epi-layers are subsequently ICP etched using the top metal layer as etch-mask. The ground metal layer is dry-etched by an Ar+ ion-beam around the patch-antenna matrix down to the Si substrate. A 100-nm-thick Si_3N_4 layer is then deposited on the Si by plasma enhanced chemical vapor deposition. To electrically connect the patch-antennas, suspended ~150-nm-wide Ti/Au (20nm/600nm) wire-bridges are fabricated by a two-step e-beam lithography process. A first resist layer is used as support after deposition, e-beam lithography and reflow, followed by a second one to define the wires by standard lift-off process. The same process is used to realize the air-bridge connecting the 2D array to the 50Ω coplanar line. The latter is deposited on the Si_3N_4 to prevent current leakage between the line's electrodes and the Si substrate.

4.2. Derivation of the electrical frequency response

If P_1 and P_2 are the incident powers generated by the two QCLs, the total optical power incident on the biased photo-conductor is given by:

$$P(t) = P_{tot}[1 + m \cdot sin(\omega)t], \tag{1}$$

where $P_{tot} = P_1 + P_2$, ω is the difference between the two optical frequencies , and $m = 2\sqrt{P_1 P_2}/P_{tot}$ is the modulation index. If R is the photodetector responsivity, the generated

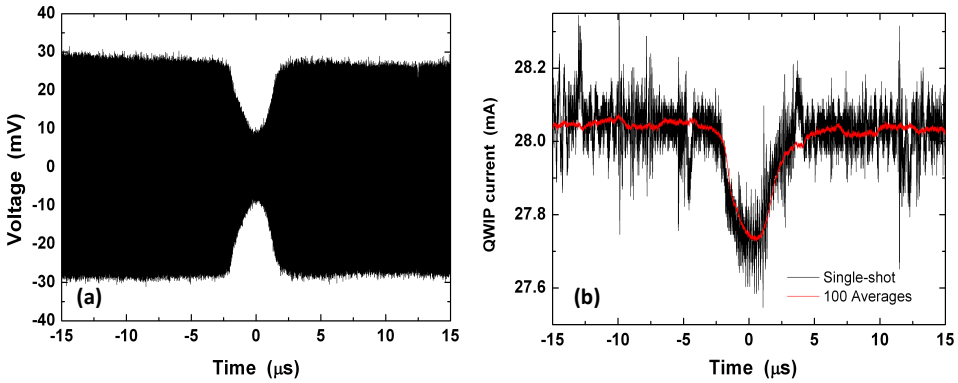

Fig. M1. Absorption dip in the time domain corresponding to the saQ(3,3) transition at a nominal pressure of 10Pa. (a) Chirped pulse in single-shot. (b) QWIP current pulse in single-shot (black) and with 100 averages (red).

photocurrent $I_{ph}(t) = R \cdot P(t)$ can be split into a dc component $I_{dc} = R \cdot P_{tot}$, which corresponds to the measured dc photocurrent, and an ac component of amplitude $I_{ac} = m \cdot R \cdot P_{tot} = m \cdot I_{dc}$. In the absence of a sizeable resistance in series with the QWIP active region, as is the case here, it can be shown that the amplitude of the current source I_s in the photodetector small signal equivalent circuit (Supplement 1) is precisely equal to $I_{ac} \simeq I_{dc}$ (since $m \simeq 1$ for the powers used in this work) [6, 45]. The electrical frequency response of the QWIP is then obtained from the expression of the average ac power dissipated in the $R_L = 50\Omega$ input impedance of the microwave power-meter:

$$P_L(\omega) = \frac{1}{2} I_{dc}^2 \left| \frac{R}{R + (R_L + i\omega L)(1 + i\omega RC)} \right|^2 R_L. \tag{2}$$

To match quantitatively the power levels obtained experimentally in Fig. 2 in the main text, we used an amplitude of the ac current source $I_s = I_{dc}/2$ where I_{dc} is the experimental dc photocurrent generated by the two QCLs ($I_{dc} = 4.1$mA, 2.8mA, and 1.25mA for devices M5, M3 and M2 respectively). However, as discussed above, ideally we would rather expect $I_s = I_{dc}$, i.e. the generated heterodyne power should be ~ 4 times higher than what found experimentally. At the moment, we don't have a clear explanation for this discrepancy, that could be in part attributed to a partial saturation of the ISB transition, each time the incident optical power oscillating at the difference frequency between the two QCLs reaches its maximum. Further measurements will be needed to validate this hypothesis.

4.3. Comparison of single-shot acquisition and pressure detection limit

In Fig.M1 we report the absorption dip in the time domain corresponding to the saQ(3,3) transition at a nominal pressure of 10Pa, obtained from the chirped pulse (panel (a)) and from the QWIP current pulse (panel (b)). The black lines were recorded in single-shot, while the red one was obtained with 100 averages (same averaging used for Fig. 5(b)). The SNRs in single-shot from the chirped and current pulse and are respectively ~ 8 and 2. From these numbers, based on the transmission intensities computed with Spectracalc®, we estimate, for our 8cm-long gas cell, a minimum detectable gas pressures in single-shot of ~ 0.3Pa and ~ 1.2Pa.

4.4. Voltage source response time

In Fig. 6, the three highest frequency NH_3 transition lines of the red spectrum (derived from the current pulse) present a systematically higher transmission compared to the green one (derived

from the heterodyne pulse), as well as a slight line asymmetry. We attribute these facts to the finite transient response time, of approximately 30μs, of the voltage source used to bias the QCL (Keithely 2440 5A SourceMeter). Indeed, from longer to shorter times (i.e. from lower to higher absolute frequencies in Fig. 6) the increase of the frequency chirp (see Fig. 4(b)), leads to progressively temporally narrower transmission dips as shown in Fig. 5(b). As a result, at some point the rise time associated to a given transition becomes too short compared to the time needed by the voltage source to change its current in order to maintain a constant bias across the QWIP. Eventually this fact prevents reaching the transmission minimum. This is clearly the case for the highest frequency transition (i.e. the temporally narrowest), for which the associated rise time is of only $\sim 10\mu$s, contrarily to the $\sim 100\mu$s of the lowest frequency one. Such experimental artifact is not present on the *ac* port of the bias-tee, where slow bias variations are filtered out.

Acknowledgments. We gratefully acknowledge Raffaele Colombelli for helpful discussions on intersubband saturation and Etienne Okada for technical support during the RF measurements.

Funding. Nord-Pas de Calais Regional Council; Fonds Européens de Développement Régional; RENATECH (French Network of Major Technology Centres); CPER "Wavetech"; Project COMPTERA - ANR 22-PEEL-0003; ANR Project BIRD.

Disclosures. The authors declare no conflicts of interest.

Supplemental document. See Supplement 1 for supporting content.

References

1. H. Schneider and H. C. Liu, *Quantum Well Infrared Photodetectors: Physics and Applications* (Springer, 2007).
2. S. Ehret, H. Schneider, J. Fleissner, P. Koidl, and G. Bohm, "Ultrafast intersubband photocurrent response in quantum-well infrared photodetectors," Appl. Phys. Lett. **71**, 641 (1997).
3. P. D. Grant, R. Dudek, M. Buchanan, and H. C. Liu, "Room-temperature heterodyne detection up to 110GHz with a quantum well infrared photodetector," Appl. Phys. Lett. **18**, 2218 (2006).
4. T. Dougakiuchi, A. Ito, M. Hitaka, K. Fujita, and M. Yamanishi, "Ultimate response time in mid-infrared high-speed low-noise quantum cascade detectors," Appl. Phys. Lett. **118**, 041101 (2021).
5. J. Hillbrand, L. M. Krüger, S. D. Cin, H. Knötig, J. Heidrich, A. M. Andrews, G. Strasser, U. Keller, , and B. Schwarz, "High-speed quantum cascade detector characterized with a mid-infrared femtosecond oscillator," Opt. Expr. **29**, 5774 (2021).
6. M. Hakl, Q. Lin, S. Lepillet, M. Billet, J.-F. Lampin, S. Pirotta, R. Colombelli, W. Wan, J. C. Cao, H. Li, E. Peytavit, and S. Barbieri, "Ultrafast quantum-well photodetectors operating at 10μm with a flat frequency response up to 70GHz at room temperature," ACS Photon. **8**, 464 (2021).
7. G. Quinchard, C. Mismer, M. Hakl, J. Pereira, Q. Lin, S. Lepillet, V. Trinite, A. Evirgen, E. Peytavit, J. L. Reverchon, J. F. Lampin, S. Barbieri, and A. Delga, "High speed, antenna-enhanced 10.3μm quantum cascade detector," Appl. Phys. Lett. **120**, 091108 (2022).
8. D. Palaferri, Y. Todorov, A. Mottaghizadeh, G. Frucci, G. Biasiol, and C. Sirtori, "Ultra-subwavelength resonators for high temperature high performance quantum detectors," New J. Phys. **18**, 113016 (2016).
9. D. Palaferri, Y. Todorov, A. Bigioli, A. Mottaghizadeh, D. Gacemi, A. Calabrese, A. Vasanelli, L. Li, A. G. Davies, E. H. Linfield, F. Kapsalidis, M. Beck, J. Faist, and C. Sirtori, "Room-temperature 9μm wavelength photodetectors and GHz-frequency heterodyne receivers," Nature **556**, 85 (2018).
10. K. L. Vodopyanov, V. Chazapis, C. C. Phillips, B. Sung, and J. S. H. Jr, "Intersubband absorption saturation study of narrow iii–v multiple quantum wells in the λ = 2.8–9 μm spectral range," Semicond. Sci. Technol. **12**, 708 (1997).
11. M. Jeannin, E. Cosentino, S. Pirotta, M. Malerba, G. Biasiol, J. Manceau, and R. Colombelli, "Low intensity saturation of an ISB transition by a mid-IR quantum cascade laser," Appl. Phys. Lett. **122**, 241107 (2023).
12. M. Jeannin, J. Manceau, and R. Colombelli, "Unified description of saturation and bistability of intersubband transitions in the weak and strong light-matter coupling regimes," Phys. Rev. Lett. **127**, 187401 (2021).
13. L. Flannigan, L. Yoell, and C.-Q. Xu, "Mid-wave and long-wave infrared transmitters and detectors for optical satellite communications—a review," J. Opt. **24**, 043002 (2022).
14. X. Pang, O. Ozolins, R. S. J. Storck, A. Udalcovs, J. R. Navarro, A. Kakkar, G. Maisons, M. Carras, G. Jacobsen, S. Popov, and S. Lourdudoss, "Gigabit free-space multi-level signal transmission with a mid-infrared quantum cascade laser operating at room temperature," Opt. Lett. **42**, 3646 (2017).
15. H. Dely, T. Bonazzi, O. Spitz, E. Rodriguez, D. Gacemi, Y. Todorov, K. Pantzas, G. Beaudoin, I. Sagnes, L. Li, A. G. Davies, E. H. Linfield, F. Grillot, A. Vasanelli, and C. Sirtori, "10 Gbit/s free space data transmission at 9um wavelength with unipolar quantum optoelectronics," Laser Photonics Rev. **16**, 2100414 (2022).
16. F. Wang, S. Slivken, and M. Razeghi, "Harmonic injection locking of high-power mid-infrared quantum cascade lasers," Photon. Res. **9**, 1078 (2021).

17. P. Didier, H. Dely, T. Bonazzi, E. A. O. Spitz, E. Rodriguez, A. Vasanelli, C. Sirtori, and F. Grillot, "High-capacity free-space optical link in the midinfrared thermal atmospheric windows using unipolar quantum devices," Adv. Photonics **4**, 056004 (2022).
18. P. Didier, H. Knötig, O. Spitz, L. Cerutti, A. Lardschneider, E. Awwad, D. Diaz-Thomas, A. N. B. R. Weih, J. Koeth, B. Schwarz, and F. Grillot, "Interband cascade technology for energy-efficient mid-infrared free-space communication," Photon. Res. **11**, 582 (2023).
19. D. Weidmann, W. J. Reburn, and K. M. Smith, "Ground-based prototype quantum cascade laser heterodyne radiometer for atmospheric studies," Rev. Sci. Instrum. **78**, 073017 (2007).
20. Y. Wang, M. G. Soskind, W. Wang, and G. Wysocki, "High-resolution multi-heterodyne spectroscopy based on Fabry-Perot quantum cascade lasers," Appl. Phys. Lett **104**, 031114 (2014).
21. N. A. Macleod, F. Molero, and D. Weidmann, "Broadband standoff detection of large molecules by mid-infrared active coherent laser spectrometry," Opt. Expr. **23**, 912 (2015).
22. A. Diaz, B. Thomas, P. Castillo, B. Gross, and F. Moshary, "Active standoff detection of CH_4 and N_2O leaks using hard-target backscattered light using an open-path quantum cascade laser sensor," Appl. Phys. B **122**, 121 (2016).
23. C. S. Goldenstein, R. M. Spearrin, J. B. Jeffries, and R. K. Hanson, "Progress in energy and combustion science," Progr. Energy Combust. Sci. **60**, 132 (2016).
24. P. Asselin, Y. Berger, T. R. Huet, L. Margules, R. Motiyenko, R. J. Hendricks, M. R. Tarbutt, S. K. Tokunagaef, and B. Darquié, "Characterising molecules for fundamental physics: an accurate spectroscopic model of methyltrioxorhenium derived from new infrared and millimetre-wave measurements," Phys.Chem.Chem.Phys. **19**, 4576 (2017).
25. A. Kawai, K. Hashimoto, T. Dougakiuchi, V. R. Badarla, T. Imamura, T. Edamura, and T. Ideguchi, "Time-stretch infrared spectroscopy," Comm. Phys. **3**, 152 (2020).
26. T. Dougakiuchi and N. Akikusa, "Application of high-speed quantum cascade detectors for mid-infrared, broadband, high-resolution spectroscopy," Sensors **21**, 5706 (2021).
27. P. L. T. Sow, S. Mejri, S. K. Tokunaga, O. Lopez, A. Goncharov, B. Argence, C. Chardonnet, A. Amy-Klein, C. Daussy, and B. Darquié, "A widely tunable 10-um quantum cascade laser phase-locked to a state-of-the-art mid-infrared reference for precision molecular spectroscopy," Appl. Phys. Lett. **104**, 264101 (2014).
28. B. Argence, B. Chanteau, O. Lopez, D. Nicolodi, M. Abgrall, C. Chardonnet, C. Daussy, B. Darquié, Y. L. Coq, and A. Amy-Klein, "Quantum cascade laser frequency stabilization at the sub-Hz level," Nat. Photon. **9**, 456 (2015).
29. H. Pires, M. Baudisch, D. Sanchez, M. Hemmer, and J. Biegert, "Ultrashort pulse generation in the mid-IR," Progr. Quantum Electron. **43**, 1 (2015).
30. D. D.S.Hale, M. Bester, W. C. Danchi, W. Fitelson, S. Hoss, E. A. Lipman, J. D. Monnier, P. G. Tuthill, and C. H. Townes, "The berkeley infrared spatial interferometer: a heterodyne stellar interferometer for the mid-infrared," Astrophys. J. **537**, 998 (2000).
31. G. Sonnabend, D. Stupar, M. Sornig, T. Stangier, T. Kostiuk, and T. Livengood, "A search for methane in the atmosphere of Mars using ground-based mid infrared heterodyne spectroscopy," J. Mol. Spectr. **291**, 98 (2013).
32. G. Bourdarot, H. G. de Chatellus, and J.-P. Berger, "Toward a large bandwidth photonic correlator for infrared heterodyne interferometry - A first laboratory proof of concept," Astron. Astrophys. **639**, A53 (2020).
33. C. A. Balanis, *Antenna Theory: Analysis and Design, 3rd Edition* (Wiley, 2005).
34. Y. Todorov, L. Tosetto, J. Teissier, A. M. Andrews, P. Klang, R. Colombelli, I. Sagnes, G. Strasser, and C. Sirtori, "Optical properties of metal-dielectric-metal microcavities in the THz frequency range," Opt. Expr. **18**, 13886 (2010).
35. M. Jeannin, T. Bonazzi, D. Gacemi, A. Vasanelli, L. Li, A. G. Davies, E. Linfield, C. Sirtori, and Y. Todorov, "Absorption engineering in an ultrasubwavelength quantum system," Nano Lett. **20**, 4430 (2020).
36. E. Rodriguez, T. Bonazzi, H. Dely, M. Mastrangelo, K. Pantzas, B. G, I. Sagnes, A. Vasanelli, Y. Todorov, and C. Sirtori, "Metamaterial engineering for optimized photon absorption in unipolar quantum devices," Opt. Expr. **30**, 20515 (2020).
37. H. A. Haus, *Waves and Fields in Optoelectronics* (Prentice Hall, 2004).
38. K. Namjou, S. Cai, E. A. Whittaker, J. Faist, C. Gmachl, F. Capasso, D. L. Sivco, , and A. Y. Cho, "Sensitive absorption spectroscopy with a room-temperature distributed-feedback quantum-cascade laser," Opt. Lett. **23**, 219 (1998).
39. M. T. McCulloch, E. L. Normand, N. Langford, G. Duxbury, and D. A. Newnham, "Highly sensitive detection of trace gases using the time-resolved frequency downchirp from pulsed quantum-cascade lasers," J. Opt. Soc. Am. B **20**, 1761 (2003).
40. E. Normand, M. McCulloch, G. Duxbury, and N. Langford, "Fast, real-time spectrometer based on a pulsed quantum-cascade laser," Opt. Lett. **28**, 16 (2003).
41. B. Grouiez, V. Zeninari, L. Joly, and B. Parvi, "Pulsed quantum-cascade-laser spectroscopy with intermediate-size pulses: application to NH_3 in the 10μm region," Appl. Phys. B **100**, 265 (2010).
42. L. Tombez, F. Cappelli, S. Schilt, G. D. Domenico, S. Bartalini, and D. Hofstetter, "Wavelength tuning and thermal dynamics of continuous-wave mid-infrared distributed feedback quantum cascade lasers," Appl. Phys. Lett. **103**, 031111 (2013).
43. M. T. Michael, N. Langford, and G. Duxbury, "Real-time trace-level detection of carbon dioxide and ethylene in car exhaust gases," Appl. Opt. **44**, 2887 (2005).
44. S. Welzel, F. Hempel, M. Hübner, N. Lang, P. B. Davies, and J. Röpcke, "Quantum cascade laser absorption

spectroscopy as a plasma diagnostic tool: An overview," Sensors **10**, 06861 (2010).
45. E. Peytavit, G. Ducournau, , and J.-F. Lampin, *"THz Photomixers," in Fundamentals of Terahertz Devices and Applications* (John Wiley & Sons, 2021).
46. J. S. Gomez-Diaz, M. Tymchenko, J. Lee, M. A. Belkin, , and A. Alú, "Nonlinear processes in multi-quantum-well plasmonic metasurfaces: electromagnetic response, saturation effects, limits, and potentials," Phys. Rev. B **92**, 125429 (2015).
47. P. Corrigan, R. Martini, E. A. Whittaker, and C. Bethea, "Quantum cascade lasers and the Kruse model in free space optical communication," Opt. Expr. **17**, 4355 (2021).

Real-time, chirped-pulse heterodyne detection at room-temperature with 100GHz 3dB-bandwidth mid-infrared quantum-well photodetectors: supplemental document

1. PATCH ARRAYS ABSORPTION SPECTRA

The devices are quantum-well infrared photodetectors (QWIPs) based on square matrices of patch-antenna resonators. For all of them the patches consist of metallic squares of lateral side $s = 1.8\mu$m. The 5×5, 3×3 and 2×2-matrix devices are labelled respectively M5, M3 and M2, and correspond to those studied in the main text. Their SEM pictures are shown in the inset of Fig.S1(a). The characterisation of an additional device, based on a 11×11 matrix, is presented in this Section. In the M5 and M3 devices (and in the 11×11 matrix device), individual patches are separated by a period $p = 5\mu$m, while for device M2 $p = 10\mu$m.

In Fig.S1(a) we report the absorption spectra, obtained with a mid-infrared (MIR) microscope coupled to a Fourier transform (FTIR) spectrometer. The microscope is equipped with an adjustable radiation blocking diaphragm that we set to form a square aperture of $\sim 25\mu$m side, in order to mimic the waist of the the focused QCLs used throughout this work. We used a polarizer to polarize the incident MIR radiation perpendicularly to the wire bridges, and therefore excite the TM_{010} mode of the patch antenna resonators oscillating in the same direction. As shown in Fig.S1(a), for all the devices the main absorption peak is centered close to 10μm wavelength and corresponds to the TM_{010} mode. We attribute the other peak close to 8μm, visible in the spectra of devices M5 (red) and M3 (blue) and on the one based on the 11×11 matrix (black), to a delocalised plasmonic mode due to the coupling between adjacent patches. This interpretation, that we did not investigate further, is in agreement with the fact that the peak disappears in the spectrum of device M2 (green), where the patches are separated by 10μm rather than 5μm, and are therefore completely uncoupled.

As expected the TM_{010} mode peak absorption is reduced by decreasing the number of patches. Indeed the excitation area roughly matches the size of the 5×5 matrix. As a consequence, for the 3×3 and 2×2 matrices part of the incident radiation is directly reflected by the metallic ground-plane. QWIP M5 itself is not exempt from reflection from the ground-plane. This is demonstrated by the absorption spectrum measured on the 11×11 matrix device, shown by the black curve in Fig.S1(a). In this case the excitation area is significantly smaller than the area covered by the patches, yielding a 96% peak absorption compared to 80% for device M5. This demonstrates that for $p = 5\mu$m we practically reach critical coupling (100% peak absorption). The choice of $p = 10\mu$m for device M2, which leads to a peak absorption of $\sim 40\%$ (on a 11×11 matrix - not shown), stems from the need to maintain, for this detector, a reasonable spatial overlap with the waist of the focused QCLs.

2. DARK CURRENT AND PHOTOCURRENT CHARACTERISTICS

In Fig.S1(b) we report, for QWIP M5, the thermally activated dark current (black) and the total current under illumination (red) at T=300K. The latter is obtained with an incident power of 32.25mW from a DFB QCL at $\lambda = 10.3\mu$m, focused with an AR coated aspheric chalcogenide lens (NA = 0.56; 5 mm focal length), yielding a waist diameter of $\sim 25\mu$m. Not surprisingly, at room-temperature the dark current is dominating over the photocurrent component. Several photocurrent *vs* bias characteristics are shown in the inset for different values of the incident power. For all of them we observe a clear saturation close to 4V, that we attribute to the onset of intervalley scattering, leading to a negative differential drift velocity. The average electric field of $\sim$ 110kV/cm ($\sim$ 4V/362nm) being much higher than the expected saturation field of

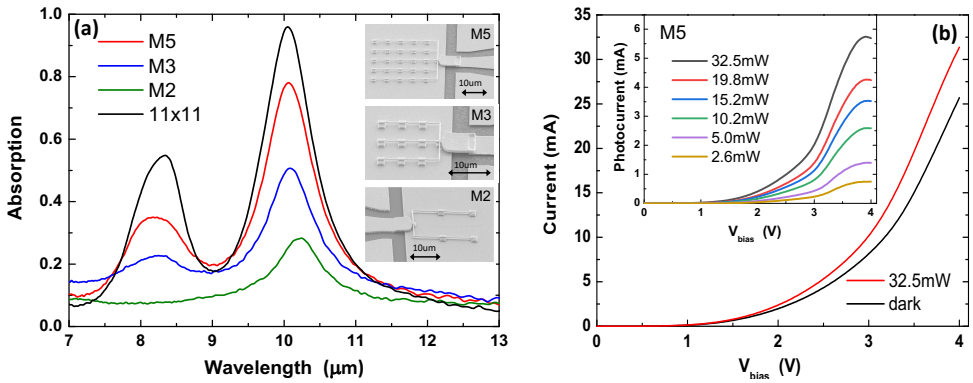

Fig. S1. (a) Room-temperature absorption spectra of QWIP photo-detectors based on square matrices of patch-antenna resonators with different number of elements. Their SEM pictures are shown on the right. In the M5 and M3 devices, individual patches are separated by a period $p = 5\mu$m, while for device M2 we used $p = 10\mu$m. As shown in the SEM pictures, patches are electrically connected together and to a 50Ω integrated coplanar line a by suspended gold wires of $\sim$ 150nm diameter. The black line corresponds to the absorption spectrum of an 11×11 matrix with $s = 1.8\mu$m and $p = 5\mu$m (same as for QWIPs M5 and M3). (b) Main panel. M5 QWIP photodetector: dark current (black) and current under illumination with an incident power of 32.5mW from a DFB QCL at $\lambda = 10.3\mu$m (red). Inset: photocurrent *vs* bias characteristics for different incident powers. All data were measured at 300K.

$10 - 20$kV/cm, indicates that the applied bias drops mostly on the Schottky contacts.

3. DERIVATION OF QWIP ABSORPTION, RESPONSIVITY AND SATURATION INTENSITY

Within the formalism of coupled mode theory (CMT), the cavity mode and the intersubband (ISB) system are modeled as coupled oscillators subject to an external excitation field. Their dynamics is described by the following equations [1]:

$$\frac{da_{isb}}{dt} = (i\omega_{isb} - \gamma_{isb})a_{isb} + i\Omega_{Rabi}a_{cav}, \tag{S1}$$

$$\frac{da_{cav}}{dt} = (i\omega_{cav} - \gamma_{nr} - \Gamma_r)a_{cav} + i\Omega_{Rabi}a_{isb} + \sqrt{2\gamma_r}s^+, \tag{S2}$$

$$s^- = -s^+ + \sqrt{2\gamma_r}a_{cav}. \tag{S3}$$

Here a_{isb}, a_{cav}, s^+, and s^- are respectively the amplitudes of the ISB and cavity oscillators (with natural frequencies ω_{isb} and ω_{cav}) and of the incoming and reflected fields. γ_{isb}, and γ_{nr} are the ISB and cavity damping rates, and γ_r is the cavity radiative damping. These rates are related to their corresponding Q-factors by the relation $\gamma_i = \omega_0/2Q_i$, with $\omega_0 = \omega_{isb}, \omega_{cav}$. Finally, the coupling between the oscillators is determined by the Rabi frequency, Ω_{Rabi}, given by:

$$\Omega_{Rabi} = \frac{1}{2}\sqrt{\frac{f_w f_{12} e^2 \Delta n}{\epsilon_0 \epsilon m^* L_{QW}}}, \tag{S4}$$

where $f_w = 0.082$ is the filling factor of the quantum wells (QWs) in the active region, $f_{12} = 0.46$ the oscillator strength of the ISB transition (corresponding to a dipole matrix element $z_{12} = 1.5$nm), $L_{QW} = 6$nm the QW thickness, and Δn_s the population difference (in cm^{-2}) between the ground state and the excited state of the ISB transition. At low excitation power $\Delta n = n_s = 3\times10^{11}$cm^{-2}, the nominal sheet doping density.

From Eqs.(S1)-(S3), with an incident field $s^+ = e^{i\omega t}$, we obtain the ISB absorption, A_{isb}, which corresponds to the external quantum efficiency, and the cavity absorption A_{cav}:

$$A_{isb}(\Delta n, \omega) = 2\gamma_{isb}\left|\frac{a_{isb}}{s^+}\right|^2 = \frac{4\gamma_r\gamma_{isb}\Omega_{Rabi}^2}{|[\gamma_{isb} + i(\omega - \omega_{isb})][(\gamma_{nr} + \gamma_r) + i(\omega - \omega_{cav})] + \Omega_{Rabi}^2|^2}, \tag{S5}$$

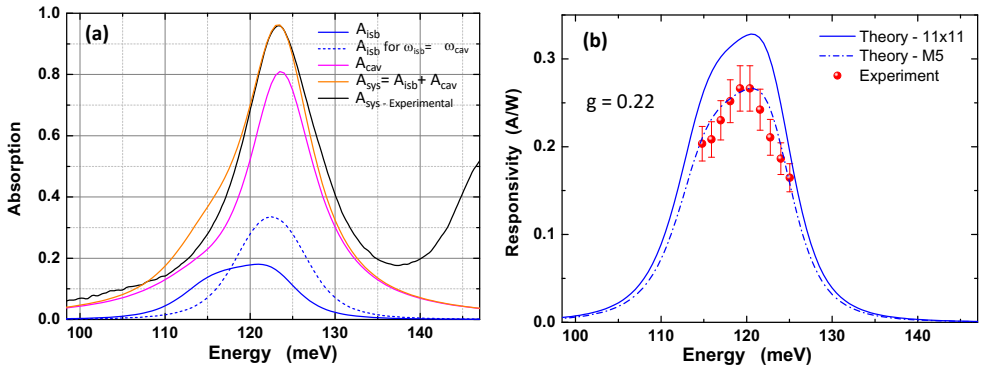

Fig. S2. (a) Computed absorption *vs* photon energy for an infinite matrix using CMT: A_{isb} (blue); A_{cav} (pink); $A_{sys} = A_{isb} + A_{cav}$ (orange). Spectra are computed using the following parameters: $\hbar\omega_{isb} = 115$meV; $\hbar\omega_{cav} = 122.5$meV; $z_{12} = 1.5$nm; $\Delta n = n_s = 3\times10^{11}$cm^{-2}; $Q_{isb} = 10$; $Q_r = 29$, and $Q_{nr} = 23.5$. The black line is the experimental absorption spectrum (same as Fig.S1(a)). The dashed blue line represents the computed external quantum efficiency, A_{isb}, in the case where $\hbar\omega_{isb} = \hbar\omega_{cav} = 122.5$meV. (b) Computed responsivity for an infinite matrix (solid line) and for device M5 (dash-dotted line) using $g = 0.22$. The red circle are the experimental points for device M5 (same as Fig.1(a) in the main text).

$$A_{cav}(\omega) = 2\gamma_{nr}\left|\frac{a_{cav}}{s^+}\right|^2 = \frac{4\gamma_r\gamma_{nr}[\gamma_{isb}^2 + (\omega-\omega_{isb})^2]}{|[\gamma_{isb} + i(\omega-\omega_{isb})][(\gamma_{nr}+\gamma_r) + i(\omega-\omega_{cav})] + \Omega_{Rabi}^2|^2}. \tag{S6}$$

From Eqs.(S5),(S6), we can compute, for $\Delta n = n_s$, the system absorption spectrum, $A_{sys} = A_{isb} + A_{cav}$, for an ISB transition energy $\hbar\omega_{isb} = 115$meV, and using $Q_{isb} = 10$ (i.e. the typical ISB Q-factor). The solid orange curve in Fig.S2(a) is the best agreement with the experimental absorption spectrum of the 11×11 matrix (solid black line - same as Fig.S1(a)) which, as explained in the previous Section, is equivalent to that obtained with an infinite matrix. The spectrum was obtained with $\hbar\omega_{cav} = 122.5$meV, $Q_r = 29$, and $Q_{nr} = 23.5$, yielding a total bare-cavity (i.e. without ISB absorption) Q-factor, $Q_{cav} = (1/Q_r + 1/Q_{nr})^{-1} = 13$. We note that the latter is very close to the value of the Q-factor (= 11) of the total system (i.e. including ISB absorption). This is a consequence of the fact that the cavity absorption, A_{cav}, (Fig.S2(a), solid pink spectrum) is significantly larger than A_{isb} (solid blue spectrum). The latter peaks at $\sim$ 120meV ($\sim 10.3\mu$m) yielding en external quantum efficiency close to 20% for the 11×11 matrix, i.e. of $\sim$ 15% for QWIP M5 (by taking into account the experimental decrease in absorption due to the larger QCL spotsize compared to the QWIP area - see red spectrum in Fig.S1).

The blue dashed line shows the computed A_{isb} in the case where the natural ISB and cavity mode frequencies are equal ($\omega_{isb} = \omega_{cav} = 122.5$meV). In this case we obtain a peak quantum efficiency of $\sim$ 35% ($\sim$ 25% for QWIP M5).

Once A_{isb} is known, the QWIP responsivity can be obtained from:

$$R = A_{isb}\frac{eg}{\hbar\omega}, \tag{S7}$$

where g is the photoconductive gain. In Fig.S2(b) we report the computed responsivity for the 11×11 matrix and for QWIP M5 obtained with $g = 0.22$, which gives a good agreement with the data (red circles, same as Fig.1(a) in the main text). This value is very close to that obtained in Ref.[2] for a similar QWIP active region ($g = 0.18$). From the value of the photoconductive gain we obtain, for QWIP M5 under an applied bias of 4V ($I_{dark} = 25$mA see Fig.S1(b)), a 300K dark-current limited specific detectivity $D^* = R\sqrt{A_{coll}/(4egI_{dark})} \sim 10^7$ Jones ($A_{coll} \sim 25\times25\mu$m^2 is the radiation collection area), close to what found in Ref.[3] for a patch-antenna QWIP of similar size.

The saturation intensity, I_{sat}, is defined as the value of incident power per unit surface at which the absorption is 50% of the low intensity value (i.e. $\Delta n = n_s/2$). It is given by [4]:

$$I_{sat} = \frac{n_s}{4}\frac{\hbar\omega N_{qw}}{\tau_{12}A_{isb}(n_s/2,\omega)}, \tag{S8}$$

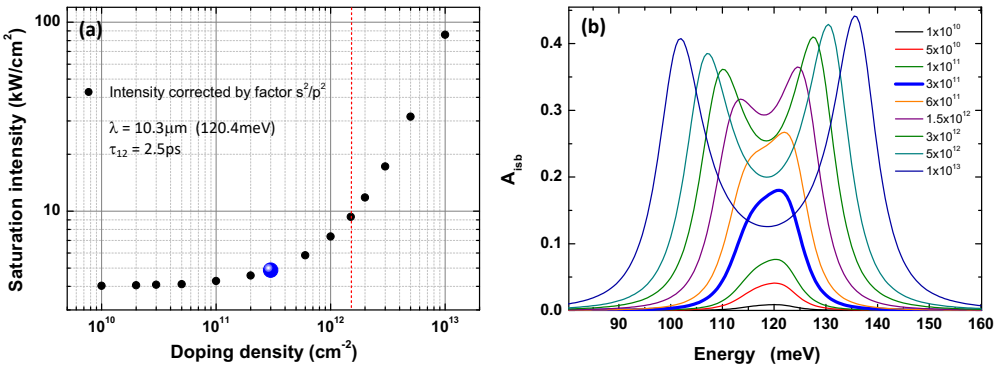

Fig. S3. Infinite matrix. (a) Saturation intensity *vs* doping density for the 11×11 matrix, at $\lambda = 10.3\mu$m. The values are obtained from Eq.(S8), multiplied by the factor s^2/p^2, with $s = 1.8\mu$m and $p = 5\mu$m. The blue dot corresponds to the nominal doping density of the QWs in the QWIP photodetectors. The dashed red line indicates approximately the transition between weak and strong coupling regimes. (b) Computed ISB absorption *vs* photon energy for the 11×11 matrix and for different doping densities. Spectra are computed with the same parameters used for Fig.S2. The thick blue line corresponds to the nominal doping density of the QWs.

where $N_{qw} = 6$ is the number of QWs in the active region, and τ_{12} is the upper state non-radiative lifetime, ruled by optical photon emission. For our structure we compute $\tau_{12} = 2.5$.

In Fig.S3(a), we report, for an infinite matrix, the expected saturation intensity as a function of n_s at $\lambda = 10.3\mu$m (120.4 meV) corresponding to the maximum responsivity (see Fig. S2(b)). To obtain this plot, the expression of I_{sat} in Eq.(S8) was actually multiplied by the ratio s^2/p^2 ($s = 1.8\mu$m, $p = 5\mu$m) to take into account the fact that each patch-antenna collects photons over an area larger than its physical surface [5]. For low doping densities the term Ω^2_{Rabi} in the denominator of Eq.(S5) can be neglected. $A_{isb}(\Delta_n, \omega)$ is therefore proportional to n_s, which makes I_{sat} independent from the doping density. Instead, at high doping $A_{isb}(\Delta_n, \omega)$ is inversely proportional to n_s, resulting into a I_{sat} proportional to n_s^2. The blue dot in Fig.S3(a) gives a saturation intensity of $\sim 4.8\text{kW}/cm^2$ for the actual doping density, $n_s = 3 \times 10^{11}\text{cm}^{-2}$. Multiplying this value by the laser spotsize and taking into account the peak absorption of each device (Fig.S1(a)) we finally obtain estimated saturation powers $P_{sat} \sim 30$mW, 45mW, and 20mW for QWIPs M5, M3 and M2 respectively.

Clearly, as shown in Fig.S3(a), the saturation power can be increased by simply increasing the doping of the QWs (although this will entail an increase of the dark current). However, at some point the QWIP enters in the so-called strong light-matter coupling regime, where single particle electronic states are replaced by upper and lower polaritonic modes [6]. As shown in Fig.S3(b), for the present device this transition occurs at doping densities of $\sim 2 - 3 \times 10^{12}\text{cm}^{-2}$, where the spectrum of the ISB absorption begins to display two clearly distinct peaks. Whether operating a QWIP in the strong coupling regime is a viable option is a question that must still be fully elucidated and which is beyond the scope of this work [7].

4. IMPEDANCE MEASUREMENTS AND SMALL SIGNAL EQUIVALENT CIRCUIT MODEL

The real and imaginary parts of the QWIPs impedance, $Z(\Omega)$, are reported in Fig.S4 in the ranges 0-110GHz and 140-220GHz. They are extracted from S_{11} parameters measured with a VNA analyzer after de-embedding the 50Ω integrated coplanar line. The measurements were done in the dark at 300K, under applied biases of 3.8V, 3.85V, and 4V for devices M5, M3, and M2 respectively. Since even at the highest incident powers the photocurrent is always a small fraction of the device dark current (see Fig.S1(b)), the values of the QWIP impedances in the dark can be considered, with good approximation, equal to those under illumination.

A precise modelling of $Z(\Omega)$ is beyond the scope of this work, and would require simulations to take into account propagation effects especially at high frequencies. The measured impedances can however be well reproduced through the simple lumped element equivalent circuit shown in the inset of Fig.S4(a), where R and C take into account the total resistance and capacitance of the patches, while L corresponds to the inductance of the interconnecting metallic wires ($R_L = 50\Omega$ is

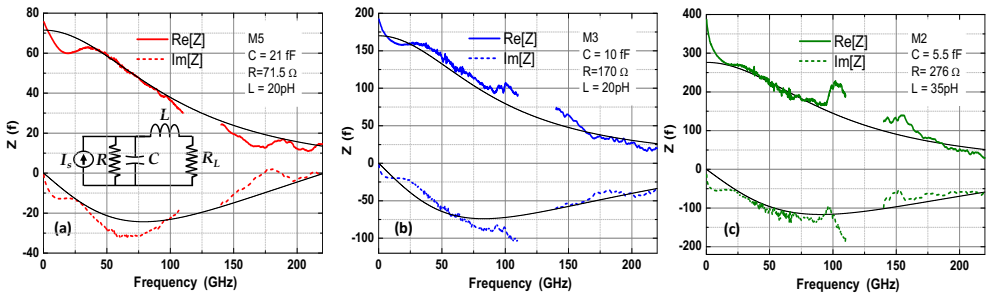

Fig. S4. Real (solid) and imaginary (dashed) parts of the QWIP impedances extracted from the S_{11} parameters measurements after de-embedding the 50Ω integrated coplanar line. The measurements were done in the dark at 300K. The black solid lines are the results of the fits obtained from the small-signal circuit reported in panel (a), with R, L and C as fitting parameters. The values obtained from the fits are reported on each panel. (a) Impedance of device M5. In the circuit, I_s is the amplitude of the current source, proportional to the *dc* photocurrent generated by the heterodyne mixing of two QCL (see main text and Appendix S2). R_L is the load impedance. (b) Impedance of device M3. (c) Impedance of device M2.

the input impedance of the power meter, while I_s is the *ac* photocurrent source). The solid black lines in Fig.S4(a),(b),(c) are the best fits of the measured impedances obtained using R, C and L as fitting parameters. As we can see the agreement is satisfactory, and the main features are correctly reproduced. As expected the resistance and capacitance scale with the number of patches. For the latter we find values of 21fF, 10fF and 5fF for devices M5, M3 and M2 respectively. These values are compatibles with the computed electrostatic capacitance of a single patch, of $\sim$ 1.1fF. The values of the inductances, of 20pH and 35pH respectively for devices M5, M3 and for device M2, are also in the right order of magnitude considering that the inductance of a 10μm-long suspended metallic wire over a ground plane (such as those connecting the patches - see Fig.S1(a)) is of $\sim$ 5pH.

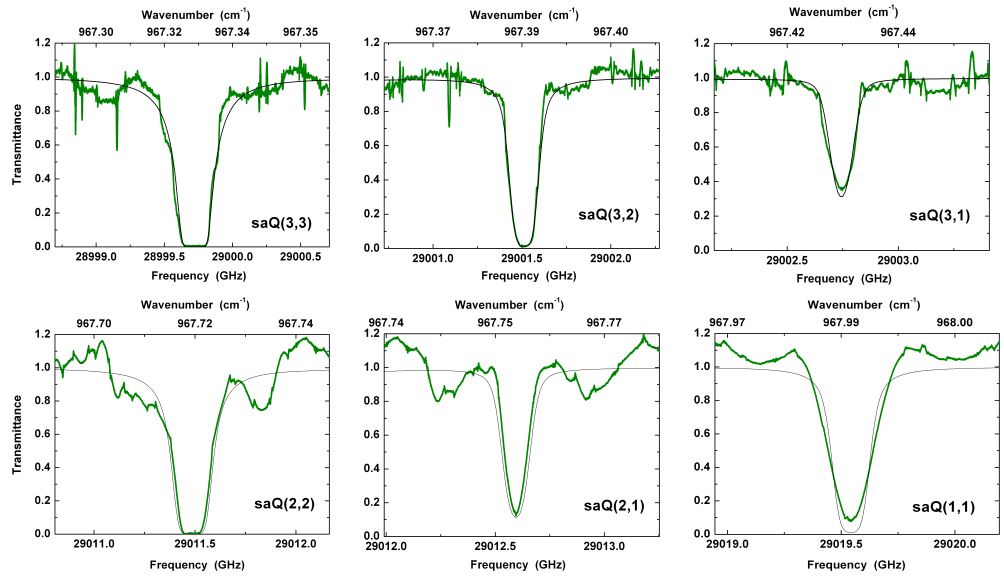

Fig. S5. Transmittances of the measured NH_3 transitions as obtained from the chirped frequency pulse (green). Computed transmittances with a pressure of 90Pa and gas cell length of 8cm (black). The line centers were shifted by the quantities shown in Table 1 of the main text.

5. NH_3 TRANSMISSION SPECTRUM.

In Fig.S5 we report a comparison between the transmittances of all the measured transitions as obtained from the chirped pulse spectrum of Fig.6 in the main text, with those computed with Spectracalc® for a NH_3 pressure of 90Pa and gas cell length of 8cm. In the computed spectra only the line centers were shifted by the quantities shown in Table 1 of the main text.

REFERENCES

1. M. Jeannin, E. Cosentino, S. Pirotta, M. Malerba, G. Biasiol, J. Manceau, and R. Colombelli, "Low intensity saturation of an isb transition by a mid-ir quantum cascade laser," Appl. Phys. Lett. **122**, 241107 (2023).
2. M. Hakl, Q. Lin, S. Lepillet, M. Billet, J.-F. Lampin, S. Pirotta, R. Colombelli, W. Wan, J. C. Cao, H. Li, E. Peytavit, and S. Barbieri, "Ultrafast quantum-well photodetectors operating at 10μm with a flat frequency response up to 70GHz at room temperature," ACS Photon. **8**, 464 (2021).
3. D. Palaferri, Y. Todorov, A. Bigioli, A. Mottaghizadeh, D. Gacemi, A. Calabrese, A. Vasanelli, L. Li, A. G. Davies, E. H. Linfield, F. Kapsalidis, M. Beck, J. Faist, and C. Sirtori, "Room-temperature 9μm wavelength photodetectors and GHz-frequency heterodyne receivers," Nature **556**, 85 (2018).
4. K. L. Vodopyanov, V. Chazapis, C. C. Phillips, B. Sung, and J. S. H. Jr, "Intersubband absorption saturation study of narrow III–V multiple quantum wells in the λ = 2.8–9 μm spectral range," Semicond. Sci. Technol. **12**, 708 (1997).
5. M. Jeannin, J. Manceau, and R. Colombelli, "Unified description of saturation and bistability of intersubband transitions in the weak and strong light-matter coupling regimes," Phys. Rev. Lett. **127**, 187401 (2021).
6. C. Ciuti, G. Bastardand, and I. Carusotto, "Quantum vacuum properties of the intersubband cavity polariton field," Phys. Rev. B **72**, 115303 (2005).
7. P.-B. Vigneron, S. Pirotta, I. Carusotto, N.-L. Tran, G. Biasiol, A. B. J.-M. Manceau, and R. Colombelli, "Quantum well infrared photo-detectors operating in the strong light-matter coupling regime," Appl. Phys. Lett. **114**, 131104 (2019).